SLOW DYNAMICS UNDER HIGH CONFINING PRESSURE IN SATURATED SANDSTONE WITH PORE PRESSURE

A NON-PEER REVIEWED PREPRINT SUBMITTED TO EARTHARXIV

Manuel Asnar[*1,2], **Christoph Sens-Schönfelder**[1], **Audrey Bonnelye**[3], **and Marco Bohnhoff**[1,2]
[1]Department of Geophysics, GFZ Helmholtz Centre for Geosciences, Potsdam, 14473, Germany
[2]Department of Earth Sciences, Freie Universität Berlin, Berlin, 12249, Germany
[3]GeoRessources Laboratory, Université de Lorraine, Nancy, 54000, France

May 15, 2026

submitted to *JASA Express Letters*

ABSTRACT

Slow dynamics is a time-dependent, nonlinear elastic behavior occurring in a variety of consolidated or damaged materials, including rocks. The influence of relative humidity and confining pressure on slow dynamics has been studied, but not that of full saturation and effective pressure. We show that slow dynamics is occurring under high confining pressure in fluid-saturated sandstone, if the effective pressure is low enough. This suggests that effective pressure determines whether slow dynamics can be observed, explaining why field observations are possible not only near the surface but also in environments with high pore pressure such as fault zones or volcanoes.

Keywords Slow Dynamics · Acoustoelasticity · Experimental Geophysics · Acoustics · Rock Physics

1 Introduction

The richness of the nonlinear elastic response of rocks makes the study of its various aspects quite challenging: hysteresis, endpoint memory, load-induced anisotropy, time-dependent changes in material properties. The current consensus leans towards there being a minimum of two concurrent effects at play, caused by different phenomena or microstructures within the rock. On one hand, behavior which can fully be described by finite strain theory using third-order elastic constants (TOEC) [Murnaghan, 1937]; on the other hand, the so-called "slow dynamics" (SD) [Ten Cate and Shankland, 1996]. SD is an intriguing feature of Earth and granular materials where strain perturbations, even of very low amplitude, will induce a sharp decrease in elastic modulus, followed by a time-dependent recovery of said modulus to its previous level as a function of the logarithm of time elapsed since the end of the perturbation [TenCate et al., 2000]. This exotic behavior, which is a part of, but not the whole, nonlinear elastic response of rocks, is sometimes also named "nonclassical nonlinear elasticity", as opposed to the "classical" nonlinear elasticity where elastic modulus is simply expanded as a power series of the strain tensor. Although it has been investigated across disciplines since the late 1980s [Guyer and Johnson, 1999, Johnson and Rasolofosaon, 1996, Ten Cate and Shankland, 1996], many properties of SD remain unclear.

The distinction between the classical and nonclassical effects has been exposed in a number of ways: separate path-dependent and independent contributions to volumetric strain [Nihei et al., 2000], different orientation-dependent and independent responses during nonlinear wave interaction experiments [TenCate et al., 2016], distinct frequency-dependent and independent nonlinear responses to Dynamic Acousto Elastic Testing (DAET) [Rivière et al., 2016], and irreconcilable differences in anisotropy [Asnar et al., 2025] all point towards a fundamental difference in nature between the classical and nonclassical effects. However, two major factors which have been thoroughly investigated in

[*]masnar@gfz.de

a classical context have seldom been looked into when it comes to SD: first, the nonclassical elastic response to full fluid saturation and pore pressurization; and second, the response of the nonclassical effects to changes in confining pressure in the presence of a pressurized pore fluid.

Experiments looking at the interplay between fluids and elastic nonlinearity have either stopped short of full saturation and pore pressure build-up [Johnson et al., 2004, Gao et al., 2022, Van Den Abeele, 2002, Yurikov et al., 2018], not distinguished between the classical and nonclassical effects [Johnson et al., 2004, Manogharan et al., 2022], or discarded the temporal SD recovery to focus on the conditioning phase [Rivière et al., 2016, Zinszner et al., 1997]. Large-strain deformation experiments in carbonate rocks at 5 % axial strain with fluid circulating and at 10 MPa pore pressure show a clear recovery signal [Brantut, 2015], but such strain levels are substantially above the elastic limit of the material. Resonance frequency shift measurements [Zinszner et al., 1997] have been carried out in an attempt to systematically compare dry and saturated samples at identical effective pressures, but the authors were not able to report the degree of conditioning in sandstones and explicitly discarded the SD recovery data. Observations [Bittner and Popovics, 2019] and modelling [Bittner and Popovics, 2021] have suggested a link between moisture migration, evaporation and adsorption along grain contacts as a driver for SD, but the fully-saturated and pressurized case was not examined. The current consensus is that relative humidity (RH) has a significant impact on the amplitude of SD. While SD has been observed in thoroughly dry and vacuumed samples [TenCate, 2011], it is also established that moderate to high levels of RH tend to amplify SD effects [Johnson et al., 2004, Gao et al., 2022, Van Den Abeele, 2002]. Conversely, there has been evidence showing that full fluid saturation may inhibit the nonclassical nonlinear response of a sample [Manogharan et al., 2022, Johnson et al., 2004]. However, to our knowledge, no dedicated study of SD under full fluid-saturated conditions has been carried out.

The effect of confining and effective pressure on the salience of SD has rarely been explicitly investigated and has most often been observed in passing. Dynamic Acoustoelastic Testing (DAET) experiments carried out on dry samples of Berea sandstone at pressures from 0.1 MPa to 30 MPa and in the microstrain range seem to indicate that the hysteresis all but vanishes around 7.5 MPa to 10 MPa [Rivière et al., 2016], and the authors propose an exponentially decreasing prevalence of SD as the confining pressure increases. This DAET experiment only monitored the conditioning of the sample and did not look at the SD recovery specifically. There was no fluid circulating through the sample nor pore pressure being applied, and it is therefore unclear whether the claimed 10 MPa is indeed a limit in confining pressure, or in effective pressure. The validity of an effective pressure law has never been tested for the nonclassical nonlinear elastic response of rocks.

Nonlinear behavior in rocks can appear at strains as low as 10^{-9}, with SD manifesting around 10^{-7} to 10^{-6} [Pasqualini et al., 2007]. DAET and Nonlinear Resonant Ultrasound (NRUS) experiments have highlighted a quasi-linear dependence of the maximum softening on the maximum driving amplitude [Rivière et al., 2016, Lebedev and Manakov, 2024, Yoritomo and Weaver, 2020].

SD has not only been observed in laboratory experiments but also at the field scale seismology as a characteristic drop in seismic velocity after the passage of seismic waves and the subsequent log-time re-increase that has been observed to last for years [Brenguier et al., 2008, Gassenmeier et al., 2016, Okubo et al., 2024]. One of the major issues in linking laboratory SD measurements and similar-looking field observations is that of pressure: if SD is only prevalent at extremely low pressures, then how can we explain postseismic logarithmic velocity recoveries? Such recoveries have been linked to water content variations in the near subsurface [Illien et al., 2022]; moreover, nonlinear elastic effects have been shown to be particularly prominent in volcanic environments. The presence of fluid-filled pores and unconsolidated pyroclastic granular material makes them particularly good candidates for nonclassical nonlinear elasticity, as shown in a seismic interferometry study spanning over 15 years in Mexico [Lesage et al., 2014]. The spatial distribution of seismic velocity variations induced by the 2011 Tohoku-Oki earthquake has been shown to not correlate with coseismic ground motion, deformation, or even proximity to the epicenter, but instead seems to be larger in known volcanic areas, which the authors explain by lower effective pressures in such regions due to the presence of pressurized volcanic fluids [Brenguier et al., 2014]. A study carried out in the subduction zone near Costa Rica reached similar conclusions and also attributed the observed velocity changes to pore fluid lowering the effective pressure of the medium, while distinguishing between shallow and deep velocity changes: while the former reach their peak immediately after a seismic event, the latter reach their maximum over the course of several days [Chaves and Schwartz, 2016]. These observations lend credence to the fact that effective pressure may be a critical factor in the observability of SD in the field, but it has never been demonstrated in a laboratory setting.

In order to go beyond studying the influence of RH and confining pressure on SD, we present an experiment carried out on a water-saturated and pressurized Bentheim sandstone sample, with the explicit goal of investigating whether SD can still be observed in fluid-saturated rocks under high confining pressure provided that the effective pressure is low enough. By measuring relative P-wave velocity changes (η) as we apply a deviatoric strain on the sample, we show that SD can still be observed despite the confining pressure being significantly higher than levels previously reported in the

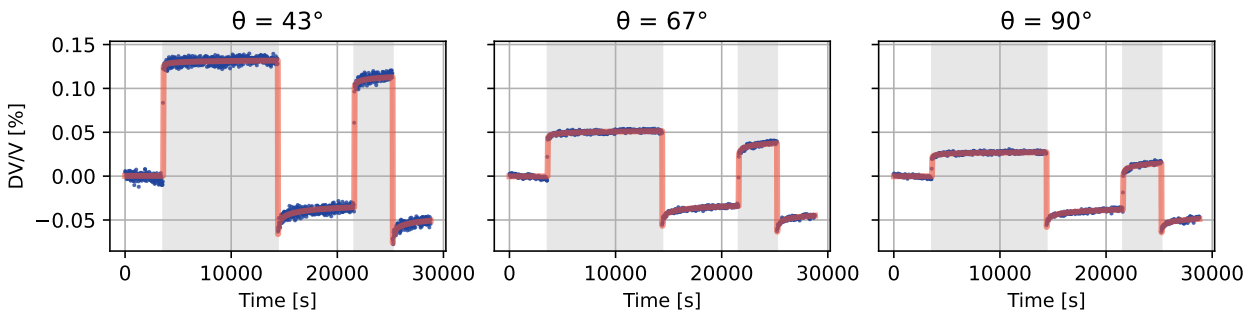

Figure 1: Three out of our 62 relative velocity change measurements, noted η, and their corresponding fits. The scatterplots are the real data with the linear component $\alpha L(t)$ removed, while the solid lines are the corresponding best model fits with our 9-component model. The grey backgrounds correspond to the *compressed* state.

literature with a comparable strain. We compare our results to a previous publication where we carried out a similar analysis on the same dry Bentheim sample [Asnar et al., 2025].

2 Experiment and results

We refer the reader to our previous publication [Asnar et al., 2025] and its corresponding Supplementary Material for a detailed account of the experimental setup, modelling, and data processing steps that were also applied here. We use a cylindrical sample of Bentheim sandstone 10 cm high and 5 cm in diameter, under a confining pressure of $P_{conf} = 25\,\mathrm{MPa}$. We also fill it with pressurized water at $P_{pore} = 23\,\mathrm{MPa}$, leading to an effective pressure $P_{eff} = 2\,\mathrm{MPa}$. We submit the sample to two displacement-controlled, axial, static cycles of loading and unloading with 20 µm vertical displacement. We refer to the periods during which the sample is under additional axial load as the *compressed* state, and the periods during which only hydrostatic pressure is applied as the *relaxed* state. The compressed phases last for 3 h and 1 h respectively, with a 2 h relaxed period between them. The compressed phases are denoted by a grey background in all figures. Relative P-wave velocity changes are monitored using ultrasonic probing every $T = 20\,\mathrm{s}$ using an array of 14 piezoelectric transducers glued to the surface of the sample. The relative velocity changes η, which we estimate from direct P-wave arrivals only, serve as a proxy for changes in the sample's dynamic Young modulus M, with $dM/M = 2dV_P/V_P = 2\eta$ [Renaud et al., 2011].

Figure 1 shows a few observations for source-receiver combinations with different angles θ between the loading axis and the P-wave ray path. While the measurements have individual noise characteristics most likely related to sensor coupling and near-sensor structure, a number of observations can be made systematically. During compression, velocities increase with larger amplitudes for smaller angles θ, meaning for paths that are closer to the loading axis. After the first increase, η often drops below zero. After load changes, a transient increase in η due to the nonclassical effect is clearly observed in the measurements.

We divide the η time series into five different segments, numbered 0 to 4, each separated by the successive axial load changes, and model each of these segments as the sum of a classical nonlinear and nonclassical nonlinear elastic component as described by

$$\eta(t,\theta) = \alpha L(t) + \sum_{i=0}^{4} \beta_i(\theta) C_i(t) + \sum_{j=1}^{4} \delta_j(\theta) R_j(t) \tag{1}$$

The components $C_i(t)$ and $R_j(t)$ are represented in Figure 2. $L(t)$ is a simple linear function, equal to 0 at $t = 0$ and 1 at $t = 8\,\mathrm{h}$, with the coefficient α accounting for a monotonous, temperature-related drift that is consistent across sensor combinations. In this experiment, $\alpha = -0.85 \times 10^{-2}\,\%$, meaning a linear drift of about $-0.11 \times 10^{-2}\,\%$ per hour. Not accounting for α as a model parameter, this yields a 9-component model. The classical components $C_i(t)$ are simply constant steps of unit amplitude over each different strain state, and zero elsewhere. The nonclassical components $R_j(t)$ are built based on an empirical recovery function R representing a superimposition of processes with different characteristic exponential recoveries [Snieder et al., 2016]

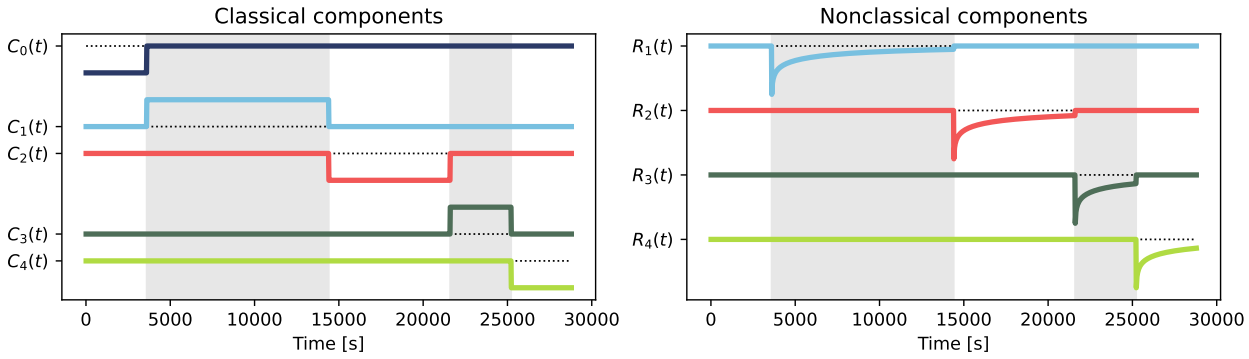

Figure 2: Base vectors for our 9-component model as given in Equation 1. The five classical components C_i are of unit amplitude over the i-th segment, and zero elsewhere, while each R_j component describes the nonclassical softening and recovery over the j-th segment. All vectors are of unit amplitude. The classical components alternate between negative and positive in order to ensure that every corresponding β coefficient is counted positive. The dashed lines are the $y = 0$ lines. There is no R_0 component, since this would be before the sample has been perturbed. The grey background corresponds to the periods where uniaxial strain is being applied on the sample on top of the hydrostatic pressure.

$$R(t) = \int_{\tau_{min}}^{\tau_{max}} \frac{1}{\tau} e^{-t/\tau} d\tau \tag{2}$$

with the particular features that $R(0) = \log(\tau_{max}/\tau_{min})$, which is a finite value, $R(t)$ converges to 0 for $t \to +\infty$, and behaves as $\log(t)$ in between. Our relaxation functions are normalized at 20 s after the load change, which corresponds to our active acoustic survey period, and each δ_j is equal to the corresponding SD-induced velocity drop.

We fit the model of Equation 1 to the data of each source-receiver pair to obtain the values of the parameters β_i and δ_j describing the amplitudes of the classical and nonclassical responses over each segment, and show the resulting parameter distributions in Figure 3. β_1 and β_3, corresponding to the classical effect under load, are spread over a much wider range than β_0, β_2 and β_4, which are gathered closer around zero in accordance with our expectations. The spread of β_1 and β_3 is due to the load-induced anisotropy of the classical effect, with values increasing the closer one gets to the loading axis, i.e., for lower θ.

The nonclassical parameters have a fairly consistent spread with a standard deviation ranging between 0.4×10^{-2} % to 0.5×10^{-2} %. Since there is no systematic angular dependence of the nonclassical effect [Asnar et al., 2025], we can average values of δ_j across all sensor combinations. In the relaxed states following unloading, the nonclassical response averages to $\delta_2 = (2.90 \pm 0.14) \times 10^{-2}$ % and $\delta_4 = (2.60 \pm 0.13) \times 10^{-2}$ % (95 % confidence). The nonclassical response to the first loading is smaller, with $\delta_1 = (1.26 \pm 0.10) \times 10^{-2}$ %, and the response to the second loading lies in the middle with an intermediate amplitude of $\delta_3 = (1.96 \pm 0.10) \times 10^{-2}$ %. Despite the differences between the different states, the nonclassical response is significantly above zero for every single one of those states. Additionally, the nonclassical signal was detected on every single sensor pair after every load change.

The nonclassical parameters are of fairly consistent amplitude across segments, with a much narrower spread than the classical effect. Every average value of δ is significantly above zero, meaning that SD is observed within our sample despite the high confining pressure. While the δ_j are relatively different from one another, ranging from 1.26×10^{-2} % to 2.9×10^{-2} %, the standard deviations are virtually the same for each, from 0.39×10^{-2} % to 0.51×10^{-2} %.

3 Discussion

The main result from the presented experiment is that the nonclassical effect is visibly occurring in this saturated sample at a confining pressure of 25 MPa. This is remarkable, since a previous study by Rivière [Rivière et al., 2016] looking at the influence of confining pressure on the prevalence of SD showed that the strain-η hysteresis loops and the softening, which are characteristic of SD, were both hardly observable at 10 MPa and disappeared entirely at 30 MPa, with an expected exponential decrease in-between. Considering that we have $P_{conf} = 25$ MPa, if confining pressure was indeed the main control of SD, we would expect SD to be all but invisible in our experiment. However, SD is clearly observed in Figure 1 as the characteristic $\log(t)$ η increase after load changes, and Figure 3 shows that the transient nonclassical signal is a significant part of the material response after every load change.

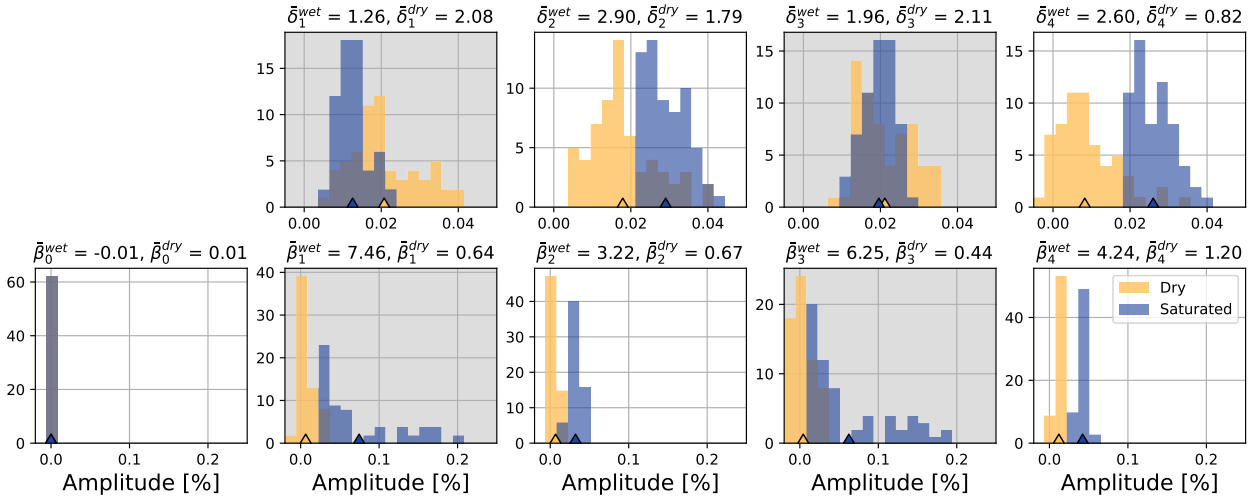

Figure 3: Distribution of each estimated model parameter for our nine-component model and comparison with the values from the dry experiment. The average value for each parameter is given and should be multiplied by a factor of 10^{-2} %. Note that the histograms for the classical and nonclassical effects have different vertical scales. Colored triangles indicate the respective average values for the saturated and dry experiments. For the dry experimental data, only parameters corresponding to direct travel paths were selected to ensure a consistent comparison.

Figure 3 shows a clear distinction in nature between the classical and nonclassical effects. β_1 and β_3, which quantify the classical velocity changes under load, are distributed in a way that matches the transverse isotropic model reasonably well (see Supplementary Material). Conversely, β_0, β_2 and β_4 are constant and clustered around zero, which is expected since there is no classical effect in the relaxed state. This is in line with the common explanation for classical nonlinear behavior: when loading (unloading), perpendicular cracks are being closed (opened), therefore increasing (decreasing) wave velocity along paths parallel to the direction of loading.

The nonclassical effect behaves in a fundamentally different way: (i) its average amplitude is consistently well below that of the classical effect; (ii) differences between compressed and relaxed states are small, with the response in the relaxed states δ_2 and δ_4 actually being more salient; (iii) anisotropy is weak (see Supplementary Material). This means that the nonclassical component can be observed for all propagation directions with slightly larger amplitudes for the relaxed states. Those observations reinforce our previous conclusions that the classical and nonclassical effects are of distinct nature.

3.1 Comparison with the dry case and the role of water

To investigate the influence of the pressurized fluid on the occurrence of SD, we compare observations presented above to the observations of the dry sample [Asnar et al., 2025] shown in Figure 3. There are three major differences between the dry and saturated experiments. The first is obviously the presence of pressurized pore fluid in the sample in the saturated case; the second is the higher $P_{conf}^{wet} = 25\,\mathrm{MPa}$ in the saturated case, compared to $P_{conf}^{dry} = 2\,\mathrm{MPa}$; and finally, the third is that the uniaxial strain $\varepsilon^{wet} = 2 \times 10^{-4}$ is four times larger than in the dry case where $\varepsilon^{dry} = 5 \times 10^{-5}$. In order to try to untangle the impact of each of these variables, let us summarize three earlier findings: (i) an increase in relative humidity usually leads to an increase in nonlinearity [Van Den Abeele, 2002, Bittner and Popovics, 2021]; (ii) an increase in confining pressure usually leads to a decrease in nonlinearity [Rivière et al., 2016]; (iii) an increase in strain amplitude usually leads to an increase in classical [Johnson and Rasolofosaon, 1996] and nonclassical [Lebedev and Manakov, 2024, Yoritomo and Weaver, 2020] nonlinearity.

Looking at the parameter values in Figure 3, two things are immediately apparent. First, the classical nonlinearity β varies over a considerably larger range of values in the saturated case compared to the dry case. Second, the nonclassical parameter values δ are of a comparable order of magnitude for the dry and saturated cases. For the classical parameter, we expect from the literature that a larger strain amplitude will induce a larger nonlinear elastic response, as the higher-order terms in the classical nonlinear elastic modulus are a direct function of strain. Therefore, given that $P_{eff}^{dry} = P_{eff}^{wet}$, the fact that $\varepsilon^{wet} = 4\varepsilon^{dry}$ induces the increase in the observed classical nonlinearity.

Perhaps not as immediately intuitive is the fact that SD in both cases is of similar magnitude. The dry experiment was performed at the same effective pressure $P_{eff} = 2\,\mathrm{MPa}$ as our saturated experiment, which may be an indication that the effective pressure is a key control of slow dynamics; however, contrary to what previous studies have suggested [Lebedev and Manakov, 2024, Yoritomo and Weaver, 2020], having a much larger strain amplitude does not seem to have increased the SD response, and the average value is not consistently larger in the dry or saturated case. The nonclassical response does seem to be higher in the saturated case than in the dry case in the compressed state only, while being lower or comparable in the relaxed state.

Most studies looking at the effects of moisture and relative humidity have indeed reported an increase in the nonlinear response with increasing moisture; in his mechanistic diffusion model, Bittner [Bittner and Popovics, 2021] suggests that the nonlinearity is highest when relative humidity reaches 100 %, as do experiments modelled using the Preisach-Mayergoyz formalism of modelling a rock as an ensemble of individual, hysteretically behaving components [Carmeliet, 2002], which has been corroborated experimentally in sandstones [Gao et al., 2022]. While our observations seem to contradict these findings, we reiterate that none of these studies have gone all the way to fully saturating the pore space within sample, and all have treated a RH of 100 % as an upper limit. Yet, one might expect a filled pore space to behave significantly differently from one where it is merely the air that is saturated.

If, as has previously been suggested, SD is indeed driven by phenomena happening at the boundaries between grains rather than in their bulk [Darling, 2004], and more specifically by friction and aging processes [TenCate, 2011, Gao et al., 2022, Asnar et al., 2025], then this would mean that it is highly sensitive to the changes in real contact area between grains. Such a real contact area can either evolve by way of indentation creep (geometric aging) [Dieterich and Kilgore, 1994], or by the formation of chemical bonds between grains (chemical aging) [Li et al., 2011]. In the case of partially humid samples, it then makes sense that increasing relative humidity in the sample would ease the sliding of grains and breaking of bonds, facilitating the conditioning effect, while also providing additional material for the creation of hydrogen bonds, therefore also easing the aging and recovery processes. This dependence of aging in silica contacts on relative humidity has been observed [McClimon et al., 2024]. However, the same study concluded that this is only true to a point: while low to moderate humidity levels drive aging processes, excessive humidity levels lead to the formation of water layers between asperities, thereby hindering the formation of bonds. Therefore, we can expect the dependence of SD on fluid presence to not be monotonous along the spectrum from 0 % RH to full fluid pressurization in the pore space: SD may start off weak, reach a peak somewhere along intermediate to high values of RH, drop back down around 100 %, and then remain weaker for full fluid saturation. In fact, measurements of the hysteretic nonlinearity coefficient carried out on Berea and Meule sandstone samples seem to follow this pattern, showing that the nonlinearity reaches a maximum around an RH of 10 % to 30 % [Van Den Abeele, 2002] before reaching a level similar to the perfectly dry case around 100 %.

In our case, we then propose that the similarity in magnitude of nonclassical effects between the dry and saturated cases is the result of two competing mechanisms: on one hand, the increased strain amplitude amplifies the nonclassical response, most likely via geometric aging; on the other hand, the pressurized fluid in the sample's pore space acts as a barrier to the chemical aging of grain contacts. We suggest that both effects act in concert such that SD is observable in the sample with pressurized pore fluid at an amplitude comparable to the dry situation.

4 Conclusion

We described the first experiment to explicitly investigate slow dynamics recovery in a fluid-pressurized Bentheim sandstone beyond the currently established limit of $P_{conf} = 10\,\mathrm{MPa}$ confining pressure. Our triaxial experiment shows that slow dynamics can still clearly be observed in fluid-saturated and pressurized sandstone under significant confining pressure, provided that the effective pressure is low enough. This provides evidence in favor of effective pressure being the relevant control for the occurrence of nonclassical nonlinear elasticity in rocks than the confining pressure. This finding supports explanations of the pronounced sensitivity of seismic velocities to strain perturbations in natural environments with pressurized pore fluids—such as fault zones and volcanic areas—as facilitated by pore pressure, counteracting the inhibiting effect of confining pressure as described by the effective pressure law. This is further confirmation for the origin of SD at grain to grain contacts.

References

F. D. Murnaghan. Finite Deformations of an Elastic Solid. *American Journal of Mathematics*, 59(2):235, April 1937. ISSN 00029327. doi:10.2307/2371405.

James A. Ten Cate and Thomas J. Shankland. Slow dynamics in the nonlinear elastic response of Berea sandstone. *Geophysical Research Letters*, 23(21):3019–3022, October 1996. ISSN 0094-8276, 1944-8007. doi:10.1029/96GL02884.

James A. TenCate, Eric Smith, and Robert A. Guyer. Universal Slow Dynamics in Granular Solids. *Physical Review Letters*, 85(5):1020–1023, July 2000. ISSN 0031-9007, 1079-7114. doi:10.1103/PhysRevLett.85.1020.

Robert A. Guyer and Paul A. Johnson. Nonlinear mesoscopic elasticity: Evidence for a new class of materials. *Physics Today*, 52(4):30–36, April 1999. doi:10.1063/1.882648.

Paul A. Johnson and Patrick N. J. Rasolofosaon. Nonlinear elasticity and stress-induced anisotropy in rock. *Journal of Geophysical Research: Solid Earth*, 101(B2):3113–3124, February 1996. ISSN 0148-0227. doi:10.1029/95JB02880.

K.T. Nihei, L.B. Hilbert, N.G.W. Cook, S. Nakagawa, and L.R. Myer. Frictional effects on the volumetric strain of sandstone. *International Journal of Rock Mechanics and Mining Sciences*, 37(1-2):121–132, January 2000. ISSN 13651609. doi:10.1016/S1365-1609(99)00098-2.

J. A. TenCate, A. E. Malcolm, X. Feng, and M. C. Fehler. The effect of crack orientation on the nonlinear interaction of a *P* wave with an *S* wave. *Geophysical Research Letters*, 43(12):6146–6152, June 2016. ISSN 0094-8276, 1944-8007. doi:10.1002/2016GL069219.

Jacques Rivière, Lucas Pimienta, Marco Scuderi, Thibault Candela, Parisa Shokouhi, Jérôme Fortin, Alexandre Schubnel, Chris Marone, and Paul A. Johnson. Frequency, pressure, and strain dependence of nonlinear elasticity in Berea Sandstone. *Geophysical Research Letters*, 43(7):3226–3236, April 2016. ISSN 0094-8276, 1944-8007. doi:10.1002/2016GL068061.

Manuel Asnar, Christoph Sens-Schönfelder, Audrey Bonnelye, Andrew Curtis, Georg Dresen, and Marco Bohnhoff. Anisotropy reveals contact sliding and aging as a cause of post-seismic velocity changes. *Nature Communications*, 16(1):7587, August 2025. ISSN 2041-1723. doi:10.1038/s41467-025-62667-0.

Paul A. Johnson, Bernard Zinszner, Patrick Rasolofosaon, Frederic Cohen-Tenoudji, and Koen Van Den Abeele. Dynamic measurements of the nonlinear elastic parameter α in rock under varying conditions. *Journal of Geophysical Research: Solid Earth*, 109(B2):2002JB002038, February 2004. ISSN 0148-0227. doi:10.1029/2002JB002038.

Linying Gao, Parisa Shokouhi, and Jacques Rivière. Effect of relative humidity on the nonlinear elastic response of granular media. *Journal of Applied Physics*, 131(5):055101, February 2022. ISSN 0021-8979, 1089-7550. doi:10.1063/5.0073967.

K. E.-A. Van Den Abeele. Influence of water saturation on the nonlinear elastic mesoscopic response in Earth materials and the implications to the mechanism of nonlinearity. *Journal of Geophysical Research*, 107(B6):2121, 2002. ISSN 0148-0227. doi:10.1029/2001JB000368.

Alexey Yurikov, Maxim Lebedev, Gennady Y. Gor, and Boris Gurevich. Sorption-Induced Deformation and Elastic Weakening of Bentheim Sandstone. *Journal of Geophysical Research: Solid Earth*, 123(10):8589–8601, October 2018. ISSN 2169-9313, 2169-9356. doi:10.1029/2018JB016003.

Prabhakaran Manogharan, Clay Wood, Chris Marone, Derek Elsworth, Jacques Rivière, and Parisa Shokouhi. Experimental Investigation of Elastodynamic Nonlinear Response of Dry Intact, Fractured and Saturated Rock. *Rock Mechanics and Rock Engineering*, 55(5):2665–2678, May 2022. ISSN 0723-2632, 1434-453X. doi:10.1007/s00603-021-02552-6.

Bernard Zinszner, Paul A. Johnson, and Patrick N. J. Rasolofosaon. Influence of change in physical state on elastic nonlinear response in rock: Significance of effective pressure and water saturation. *Journal of Geophysical Research: Solid Earth*, 102(B4):8105–8120, April 1997. ISSN 0148-0227. doi:10.1029/96JB03225.

Nicolas Brantut. Time-dependent recovery of microcrack damage and seismic wave speeds in deformed limestone. *Journal of Geophysical Research: Solid Earth*, 120(12):8088–8109, December 2015. doi:10.1002/2015jb012324.

J. A. Bittner and J. S. Popovics. Direct imaging of moisture effects during slow dynamic nonlinearity. *Applied Physics Letters*, 114(2):021901, January 2019. ISSN 0003-6951, 1077-3118. doi:10.1063/1.5063904.

J.A. Bittner and J.S. Popovics. Mechanistic diffusion model for slow dynamic behavior in materials. *Journal of the Mechanics and Physics of Solids*, 150:104355, May 2021. doi:10.1016/j.jmps.2021.104355.

James A. TenCate. Slow dynamics of earth materials: An experimental overview. *Pure and Applied Geophysics*, 168 (12):2211–2219, March 2011. doi:10.1007/s00024-011-0268-4.

Donatella Pasqualini, Katrin Heitmann, James A. TenCate, Salman Habib, David Higdon, and Paul A. Johnson. Nonequilibrium and nonlinear dynamics in Berea and Fontainebleau sandstones: Low-strain regime. *Journal of Geophysical Research*, 112(B1):B01204, January 2007. ISSN 0148-0227. doi:10.1029/2006JB004264.

A. V. Lebedev and S. A. Manakov. Experimental Study of Slow Sound Speed Relaxation in Carbonate Rocks. *Acoustical Physics*, 70(2):368–386, April 2024. ISSN 1063-7710, 1562-6865. doi:10.1134/S1063771024601638.

John Y. Yoritomo and Richard L. Weaver. Slow dynamic nonlinearity in unconsolidated glass bead packs. *Physical Review E*, 101(1):012901, January 2020. ISSN 2470-0045, 2470-0053. doi:10.1103/PhysRevE.101.012901.

F. Brenguier, M. Campillo, C. Hadziioannou, N. M. Shapiro, R. M. Nadeau, and E. Larose. Postseismic Relaxation Along the San Andreas Fault at Parkfield from Continuous Seismological Observations. *Science*, 321(5895): 1478–1481, September 2008. ISSN 0036-8075, 1095-9203. doi:10.1126/science.1160943.

M. Gassenmeier, C. Sens-Schönfelder, T. Eulenfeld, M. Bartsch, P. Victor, F. Tilmann, and M. Korn. Field observations of seismic velocity changes caused by shaking-induced damage and healing due to mesoscopic nonlinearity. *Geophysical Journal International*, 204(3):1490–1502, March 2016. ISSN 0956-540X, 1365-246X. doi:10.1093/gji/ggv529.

Kurama Okubo, Brent G. Delbridge, and Marine A. Denolle. Monitoring Velocity Change Over 20 Years at Parkfield. *Journal of Geophysical Research: Solid Earth*, 129(4):e2023JB028084, April 2024. ISSN 2169-9313, 2169-9356. doi:10.1029/2023JB028084.

Luc Illien, Christoph Sens-Schönfelder, Christoff Andermann, Odin Marc, Kristen L. Cook, Lok B. Adhikari, and Niels Hovius. Seismic Velocity Recovery in the Subsurface: Transient Damage and Groundwater Drainage Following the 2015 Gorkha Earthquake, Nepal. *Journal of Geophysical Research: Solid Earth*, 127(2):e2021JB023402, February 2022. ISSN 2169-9313, 2169-9356. doi:10.1029/2021JB023402.

Philippe Lesage, Gabriel Reyes-Dávila, and Raúl Arámbula-Mendoza. Large tectonic earthquakes induce sharp temporary decreases in seismic velocity in Volcán de Colima, Mexico. *Journal of Geophysical Research: Solid Earth*, 119(5):4360–4376, May 2014. ISSN 2169-9313, 2169-9356. doi:10.1002/2013JB010884.

F. Brenguier, M. Campillo, T. Takeda, Y. Aoki, N. M. Shapiro, X. Briand, K. Emoto, and H. Miyake. Mapping pressurized volcanic fluids from induced crustal seismic velocity drops. *Science*, 345(6192):80–82, July 2014. ISSN 0036-8075, 1095-9203. doi:10.1126/science.1254073.

Esteban J. Chaves and Susan Y. Schwartz. Monitoring transient changes within overpressured regions of subduction zones using ambient seismic noise. *Science Advances*, 2(1):e1501289, January 2016. ISSN 2375-2548. doi:10.1126/sciadv.1501289.

G. Renaud, M. Talmant, S. Callé, M. Defontaine, and P. Laugier. Nonlinear elastodynamics in micro-inhomogeneous solids observed by head-wave based dynamic acoustoelastic testing. *The Journal of the Acoustical Society of America*, 130(6):3583–3589, December 2011. ISSN 0001-4966, 1520-8524. doi:10.1121/1.3652871.

Roel Snieder, Christoph Sens-Schönfelder, and Renjie Wu. The time dependence of rock healing as a universal relaxation process, a tutorial. *Geophysical Journal International*, 208(1):1–9, October 2016. doi:10.1093/gji/ggw377.

J. Carmeliet. Application of the Preisach-Mayergoyz space model to analyze moisture effects on the nonlinear elastic response of rock. *Geophysical Research Letters*, 29(7):1144, 2002. ISSN 0094-8276. doi:10.1029/2001GL014243.

Timothy W. Darling. Neutron diffraction study of the contribution of grain contacts to nonlinear stress-strain behavior. *Geophysical Research Letters*, 31(16), 2004. doi:10.1029/2004gl020463.

James H. Dieterich and Brian D. Kilgore. Direct observation of frictional contacts: New insights for state-dependent properties. *Pure and Applied Geophysics PAGEOPH*, 143(1-3):283–302, 1994. ISSN 0033-4553, 1420-9136. doi:10.1007/BF00874332.

Qunyang Li, Terry E. Tullis, David Goldsby, and Robert W. Carpick. Frictional ageing from interfacial bonding and the origins of rate and state friction. *Nature*, 480(7376):233–236, November 2011. doi:10.1038/nature10589.

J. Brandon McClimon, Zhuohan Li, Khagendra Baral, David Goldsby, Izabela Szlufarska, and Robert W. Carpick. The Effects of Humidity on the Velocity-Dependence and Frictional Ageing of Nanoscale Silica Contacts. *Tribology Letters*, 72(4):105, December 2024. ISSN 1023-8883, 1573-2711. doi:10.1007/s11249-024-01904-x.

Leon Thomsen. Weak elastic anisotropy. *GEOPHYSICS*, 51(10):1954–1966, October 1986. ISSN 0016-8033, 1942-2156. doi:10.1190/1.1442051.

Supplementary Material

Anisotropy fits for the saturated data

In order to quantify the load-induced anisotropy of the 9 coefficients, we fit them to a cosine-squared law inspired by the Thomsen anisotropy coefficients [Thomsen, 1986], but also by the expected load-induced anisotropy of the classical effect as predicted by finite strain theory [Johnson and Rasolofosaon, 1996]. Each model parameter is fit by

$$\begin{aligned} \beta_i(\theta) &= u_i^C \cos^2(\theta) + v_i^C \\ \delta_j(\theta) &= u_j^{NC} \cos^2(\theta) + v_j^{NC} \end{aligned} \tag{3}$$

and the corresponding fits are shown in Figure 4. This is the same anisotropy analysis which was carried out in our previous study [Asnar et al., 2025]. For consistency, we perform the anisotropy analysis in this Supplementary Material using both direct and reflected P-wave arrivals, even though we only use direct arrivals in our main manuscript. In accordance with our previous study, we observe a clear difference in nature between the classical and nonclassical effects: while the classical parameters β_1 and β_3 are strongly anisotropic, as expected since they describe the state of the sample under axial load, the anisotropy of the nonclassical parameters is much less clear and borderline nonexistent. It is worth noting that δ_1 and δ_3 seem to be lower in amplitude; however, Figure 3 in our main manuscript shows only distinctly positive values of δ, meaning that negative or near-zero values of δ were overwhelmingly from reflected waves; this is also clearly apparent from Figure 4. The results from the anisotropy analysis in this Supplementary Material are most likely contaminated by some issues arising from including the such paths, but are still conclusive in showing the difference in anisotropies between the classical and nonclassical effects.

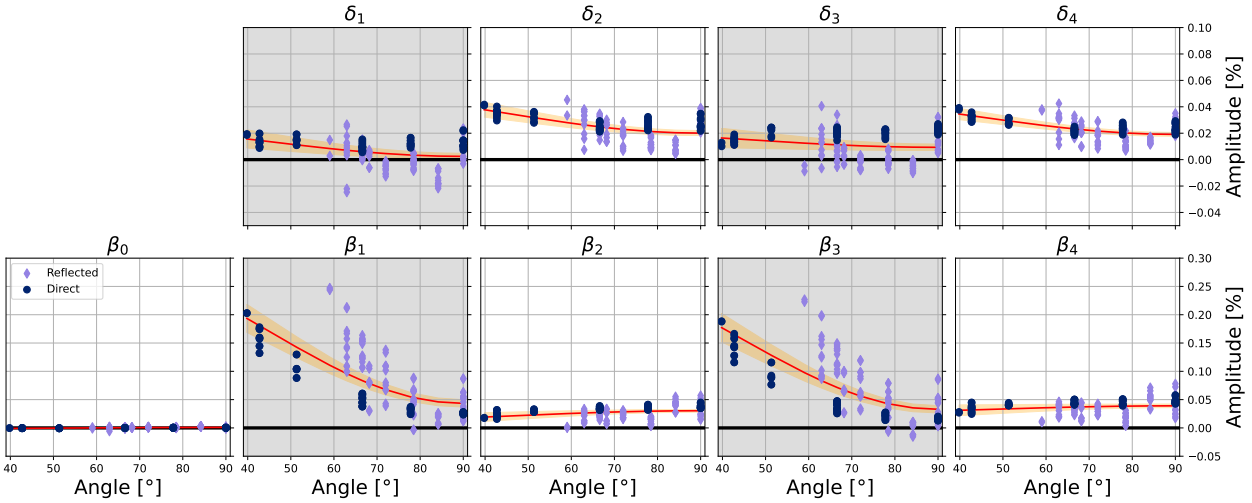

Figure 4: **Anisotropy of the nine inverted classical and nonclassical model components**. The orange envelope designates the 95 % confidence interval for each inverted model after a 5000-iteration bootstrap sampling procedure. Note the different amplitude scales between the classical and nonclassical effects. Dark circles represent the direct wave paths; light diamonds are for reflected wave paths.